



HAL
open science

Experimental analysis of rock fragmentation induced by single percussive impact

Jorge Aising, Laurent Gerbaud, Hedi Sellami

► **To cite this version:**

Jorge Aising, Laurent Gerbaud, Hedi Sellami. Experimental analysis of rock fragmentation induced by single percussive impact. *International Journal of Rock Mechanics and Mining Sciences*, 2024, 181, pp.105843. 10.1016/j.ijrmms.2024.105843 . hal-04710525

HAL Id: hal-04710525

<https://hal.science/hal-04710525v1>

Submitted on 26 Sep 2024

HAL is a multi-disciplinary open access archive for the deposit and dissemination of scientific research documents, whether they are published or not. The documents may come from teaching and research institutions in France or abroad, or from public or private research centers.

L'archive ouverte pluridisciplinaire **HAL**, est destinée au dépôt et à la diffusion de documents scientifiques de niveau recherche, publiés ou non, émanant des établissements d'enseignement et de recherche français ou étrangers, des laboratoires publics ou privés.



Distributed under a Creative Commons Attribution 4.0 International License



Experimental analysis of rock fragmentation induced by single percussive impact

Jorge Aising^{a,b,*}, Laurent Gerbaud^a, Hedi Sellami^a

^a Mines Paris, PSL Research University, Centre de Géosciences, Fontainebleau, France

^b Drillco Tools S.A., Santiago, Chile

ARTICLE INFO

Keywords:

Rock indentation
Spherical indenter
DTH hammer
Specific energy
Stress wave
Side cracks

ABSTRACT

Understanding fractures creating process during the dynamic indentation of a spherical carbide insert is a key factor to optimize the operation of a percussive drilling system and improve penetration rates and tool life while drilling in hard, abrasive rock formations. This study presents experimental results of dynamic indentation tests with combined action of an impulsive load and a static load of a bit using a single spherical carbide insert on five types of rocks. A dedicated and innovative experimental setup using a gas-gun drop test was developed to reproduce the loading forces and mechanical characteristics of a Down-the-Hole (DTH) hammer drill. A high-speed camera was used to visually determine when the major fractures, such as radial and side cracks, coalesced to create large fragments and to determine the bit displacement curve during the whole indentation process by tracking the end of the bit. To characterize the damage in the rocks, the mass of the fragments was weighed, and the Specific Energy (SE) was calculated. Experimental results showed a strong correlation between the major changes in the slope of the stress signals recorded in the drill bit and the major fragmentation events recorded with the high-speed camera. In the granites, large fragments typically associated to side cracks were generated during the loading phase. In contrast, in the limestone and the sandstone, the fragments were generated during the unloading phase. Finally, it was found that in granites, the earlier the side cracks occur relative to the maximum indentation time, the lower the efficiency of the indentation.

1. Introduction

Down The Hole (DTH) rotary percussive drilling is a widely used method for drilling in medium to hard rocks at shallow depths. The principle of operation of these hammers is based on a piston that directly impacts a drill bit capable of sliding axially within a casing. The bit is in direct contact with the rock by means of a number of tungsten carbide inserts distributed on its frontal face. The impact generates a compressive stress wave that is transmitted to the rock through the inserts, resulting in the formation of cracks and fragments of different sizes. To ensure that the drill string moves at a rate consistent with the damaged material generated by the successive impacts, a feed force, typically known as Weight On Bit (WOB), must be applied on the rotary head unit. Unlike rotary drilling, this force is not permanently applied onto the bit because during the indentation process the bit has a relative motion with respect to the casing. A comprehensive explanation of the working principle of a DTH hammer can be found in Chiang et al.¹

While DTH hammers offer advantages in terms of efficient energy

usage over other rotary percussive methods such as Top Hammer Drill (THD), several factors negatively affect the drilling rate as the hole depth increases. Significant efforts, both theoretical and experimental, have been dedicated to determine how to enhance the efficiency of energy transmission from the piston to the drill bit and from the drill bit to the rock, as these energy exchanges are where most of the energy is dissipated. Purely theoretical lumped mass models demonstrate that there exists an optimal piston length for maximizing the energy absorbed by the rock, which varies depending on the bit mass and the apparent stiffness of the rock.^{2–6} For such models to be effectively used in quantitatively predicting hammer performance, they must be coupled with empirical rock tests or advanced models such as the combined Finite-Discrete Element Method (FDEM), in order to establish a correlation between the model outputs and the mass of the fragments created. Numerous experiments have been conducted for this purpose, and a comprehensive summary of them can be found in Wu et al.⁷ These experiments can be broadly categorized into two branches: quasi-static indentations and dynamic indentations. The primary distinction

* Corresponding author. Mines Paris, PSL Research University, Centre de Géosciences, 35 rue St Honoré, 77300, Fontainebleau, France.

E-mail address: jorge.aising@minesparis.psl.eu (J. Aising).

<https://doi.org/10.1016/j.ijmms.2024.105843>

Received 25 October 2023; Received in revised form 5 July 2024; Accepted 27 July 2024

Available online 14 August 2024

1365-1609/© 2024 The Authors. Published by Elsevier Ltd. This is an open access article under the CC BY license (<http://creativecommons.org/licenses/by/4.0/>).

between them lies in the strain rate at which the rock is loaded. The ongoing debate regarding whether to use dynamic or quasi-static experiments to characterize DTH hammers is based on two distinct visions. On one hand, some authors consider DTH hammer drilling as a quasi-static process. This is founded on either the fact that the impact velocity is only a fraction of the sound velocity in the rock,^{8,9} or that the rate dependency becomes irrelevant due to the limited rock volume being loaded.^{10–12} Conversely, another group of authors consider that the strain rate falls within the range of the well-documented dependency of the rock strength under higher loading strain rates.^{13–16} As a result, they argue that it should be integrated into the constitutive rock model or in the damage rock model.^{17–21} Among these, dynamic experiments have confirmed that the efficiency of a single impact is strongly influenced by the loading conditions, the piston geometry, the length and mass ratios between the piston and the bit, and the shape of the carbide inserts.^{22–24} Unfortunately, few authors have been able to employ piston/bit length ratios similar to those in DTH hammers mainly due to the inherent constraints in the setup used. For instance, researchers such as Saksala¹⁹ and Mardoukhi,²⁵ who utilized Split Hopkinson Pressure Bar (SHPB) apparatus, were compelled to use bits at least twice as long as the piston; otherwise, they would be unable to effectively isolate the stress wave reflected by the rock.²⁶ Jiang H. et al.,^{27,28} impacted rocks by dropping a piston onto a bit with an impact energy of 417.7 J per insert, achieved by increasing the piston mass while maintaining the impact velocity below 5.33 m/s. This is in contrast to typical DTH hammers, which generally operate at around 10 m/s,¹² or more broadly, in a range between 7 and 12 m/s. Furthermore, in other test-type experiments, bits have been dropped or fired directly onto the rock, completely modifying the initial strain rate conditions of the indentation process compared to that of a hammer, in which the initial velocity of the bit just before the impact is zero.^{29–31} In tests of this nature, it becomes evident that modifying the loading conditions could also yield corresponding alterations in the results due to the dependency of the mechanical properties of rock on the strain rate.

Hence, to accurately assess the potential damage caused by a DTH hammer on various types of rocks, it becomes imperative that the length, mass, and initial loading conditions are tested as close as possible to real conditions. Otherwise, many of the aforementioned factors can significantly affect the results. Additionally, the WOB should be carefully considered, as this force can alter the stress distribution under the insert in accordance with Hertz contact theory³² or modify the apparent stiffness of the bit-rock interface³³ by compacting the rock powder trapped under the insert.³⁴ Numerous studies have highlighted its fundamental role in drilling operations, and the existence of an optimal WOB has been reported both empirically and theoretically.³⁵

A final relevant aspect to consider when describing damage caused by dynamic indentations is the generation of large fragments which have been observed both in field and laboratory tests. Understanding the mechanism that drives the generation of those fragments is of high relevance since, according to all authors involved in the topic, the energy used to generate them is relatively low given that they are created by a specific type of crack that nucleate by tensile or a combination of tensile and shear stresses.^{7,36} The name of this crack is not standardized, and references may be found as lateral crack,²⁷ transverse crack,²⁸ side crack,³⁷ or lateral vents.³⁸ Regardless of the name, the common characteristics of these cracks are that they are generated beneath the crushed zone, that they run parallel or slightly angled to the surface, and that in the case they reach the surface, they will generate the aforementioned large fragments. Hereafter, we have adopted the name side cracks, following the nomenclature used by Wu et al.⁷ Interestingly, there is still no consensus about the stage on the indentation at which these cracks are generated. Lawn et al.³² point out that side cracks occur at the unloading phase of the indentation by means of quasi-static indentation tests on brittle and amorphous materials such as soda-lime glass. Saksala³⁹ described using simulations that side cracks occur in the unloading stage due to the closure of the median crack system,

ascribing to the work of Chiang et al.⁴⁰ who —by performing simulations using a plasticity cavity model— obtained that the residual tensile stress magnitude is larger than the tensile peak during loading, indicating a greater probability for the development of side cracks during unloading. On the contrary, Shaoquan,⁴¹ by analyzing the effect of pre-existing flaws in different rock types, found that side cracks can occur during the loading stage from any of these pre-existing flaws due to the volumetric change of the fractured zone. Liu et al.³⁷ also deduced, by analyzing the power of the acoustic emissions, that the entire fracturing process occurs during the loading, and therefore, also the side cracks.

As described, many questions persist regarding the fracture dynamics of rocks when subject to dynamic indentations, especially under loading conditions and geometrical relationships representative of DTH hammers. The research presented in this paper provides significant insights into critical aspects, notably the precise timing of different fracture types in relation to the rock nature.

This paper is structured as follows: First, we provide an overview of the experimental program with a brief description of the experimental setup, a description of the tested rocks, and a description and analysis of an indentation experiment. Data processing and how the stress and displacement curves of the bit are paired with fracture events are described for some characteristic cases in section 3. Finally, in section 4, we analyze the results, draw conclusions, and outline future works.

2. Experiment description

2.1. Experimental setup

The primary objective of this work is to characterize the evolution of the fragmentation process resulting from a single impact of a piston on a bit equipped with a single insert, faithfully representing the loading conditions and geometrical relationships of a percussive DTH hammer. Specifically, in testing and designing the piston and bit used, we utilized impact velocities and impact energies (both simultaneously), piston-to-bit length and mass ratios that were as close as possible to an actual DTH hammer, with all variables scaled to a single insert. We recognize that DTH hammer operations are more complicated than what this experiment conducted under controlled conditions can reproduce, and that other factors, such as multiple impacts, the interaction between multiple inserts in a real bit, rotational torque, flushing, and the previous state of the rock, may have a large influence.^{12,21} However, the inclusion of these factors greatly complicates the elemental understanding of the underlying fragmentation mechanism. In fact, understanding the elemental interaction between a single insert and the rock is the basis for building or calibrating numerical models to evaluate more complex conditions that are difficult to address in laboratory tests.⁴² To accomplish this, we meticulously designed and assembled an experimental apparatus of the vertical gas gun type. Fig. 1(a) shows schematically the experimental setup and Fig. 1(b) shows a picture of a part of the assembly.

To record the stress signals in the bit during the indentation, a pair of strain gauges were affixed 180° apart in the center of the bit body. We used this arrangement since, as noted in Chiang,⁴³ it is expected that given the slenderness ratio of the bit, bending may occur. Similarly, we did not opt to use the two point strain gauges method, as in Karlsson,²³ since as noted in Chiang,⁴³ and later corroborated by Hashiba et al.,⁴⁴ the method for recovering the reflected signal becomes increasingly unreliable due to its susceptibility to noise. The drawback of this setup, due to the bit and piston lengths used, is that only a fraction of the reflected stress wave carrying the rock response is observed on the strain gauges. Nevertheless, a scheme similar to the one presented in Hustrulid⁴⁵ or Chiang⁴³ can be used to isolate the rock response. The strain gauge signals are later amplified by a differential amplifier and recorded with a digital oscilloscope. The impact velocity can be adjusted between 6 m/s and 14 m/s by varying the pressure at which the piston is fired.

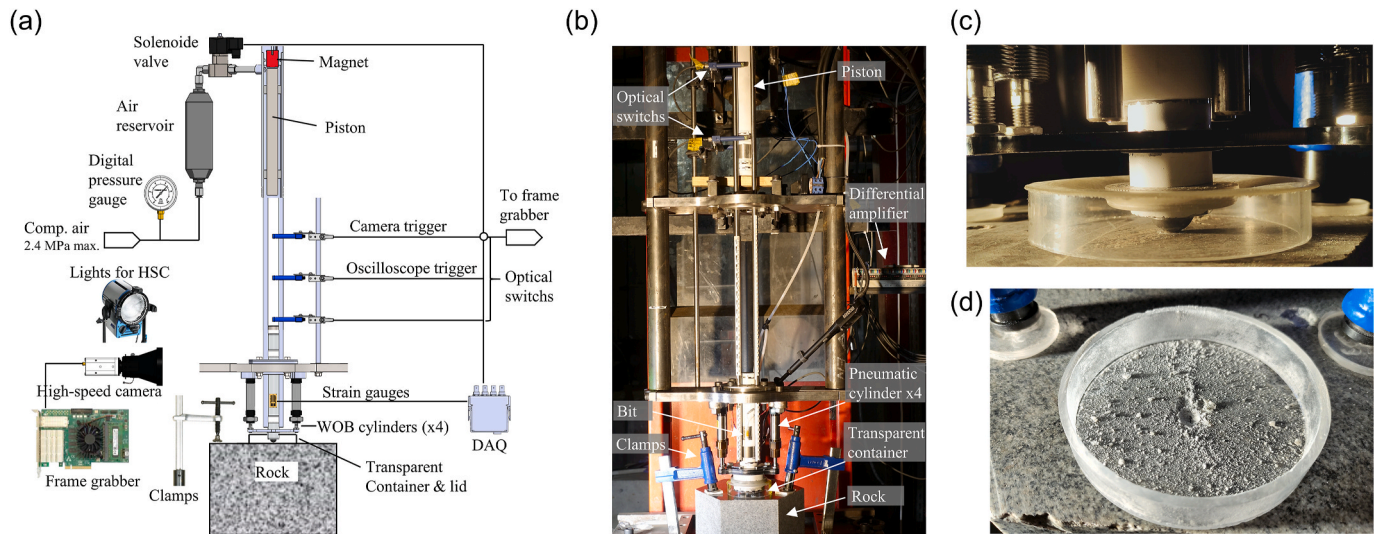


Fig. 1. (a) Schematic representation of the experimental setup. (b) Picture of part of the assembly. (c) Photograph illustrating the working position of the container and the lid in relation to the rock and the bit. (d) Photograph showing the fragments on the rock surface held in place by the transparent polycarbonate rock container prior to weighing.

Additionally, for cases where lower impact energies need to be examined, the setup accommodates free flight drops of up to 1.5 m, allowing for impacts at velocities below 5.4 m/s. Both the piston and the bit were manufactured with high strength steel with wave velocity propagation $c = 5200$ m/s and a density $\rho = 7850$ kg/m³.

To account for the effect of the pulldown, four pneumatic cylinders can apply a WOB of up to 1400 N, which is approximately twice the recommended weight per insert in DTH hammers. The position where the WOB is applied also mimics the relative position where the WOB is applied on a real bit, that is, only the first third of the bit is slightly in compression, while the remaining portion is stress-free before the impact. To calculate the impact and rebound velocity of the piston, photoelectric sensors have been arranged at a known distance. A high-speed camera records the indentation process with up to 12,000 frames per second. This allows us to visualize the interaction between the carbide insert and the rock, clearly capturing the different rock behaviors. To prevent loss of fragments, while still allowing video recording, a translucent polycarbonate container was placed on the rock surface to avoid the ejection of fragments. Furthermore, the inclusion of a lid with a central aperture atop the container facilitates a near frictionless indentation, thereby preventing the loss of fragments from the top. Fig. 1(c) depicts the operating position of the container and the covering lid in relation to the rock and the bit. The dust created during the indentation was guaranteed to be kept inside the container by the sealing action of an o-ring. By collecting all the fragments and dust, the weight of the crater mass was obtained, and the volume of the crater was calculated using the density of the rock. A high precision scale (± 0.001 g) was used for this purpose. Fig. 1(d) shows the fragments and dust resting on the rock surface, illustrating the effect of the polycarbonate container. A couple of clamps held the rock sample in place.

By tracking the bit end, the indentation versus time curve can be reconstructed. Additionally, the impact and rebound curve of the piston can be determined by focusing the camera on the impact zone between the piston and bit. Graphs containing all the essential data required for thorough characterization of the indentation process can be obtained by composing the piston displacement curve, the bit displacement curve, and the bit stress-time signal. Section 2.4 provides a concise description of this process.

2.2. Rocks tested

Five rocks typically drilled by DTH hammers due to their high

mechanical strength were tested at Mines Paris laboratory in Pau, France. The set of rocks included three heterogeneous igneous hard rocks: Red Bohus granite (RG) from the Bohuslän region in Sweden with a density of 2624 kg/m³, Sidobre granodiorite (SG) from the Sidobre region in central France with a density of 2609 kg/m³, and Kuru Grey granite (KG) with a density of 2620 kg/m³. These rocks exhibit feldspar grain sizes ranging from 1.5 to 10 mm and Unconfined Compressive Strength (UCS) ranging from 126 MPa to 192 MPa. Additionally, the set of rocks included a Saint Anne carbonated limestone (SL) extracted from quarries in southern France with a grain size of 0.4 mm, a density of 2692 kg/m³, and an average UCS of 91 MPa, as well as a very fine-grained Rhune sandstone (RS) extracted from the Basque Country in France with a density of 2670 kg/m³ and an average UCS of 129 MPa. Fig. 2(a) shows the average Unconfined Tensile Strength (UTS) against UCS for the set of rocks tested. The value in parentheses denotes the grain size. Fig. 2(b) depicts the dispersion in both UTS and UCS, where available, from which the averages were calculated. Both UTS and UCS were obtained following the International Society for Rock Mechanics (ISRM) suggested method.⁴⁶

The specimens were cut using a saw from hexagonal blocks in shape with a 25 cm circumscribed circle, except for specimens of Rhune sandstone, which were 35 cm hexagonal shape. The final height of the specimens ranges from 12 cm to 15 cm. The upper and lower faces were milled to ensure parallelism between them and the perpendicularity to the vertical axis of the impact setup. Furthermore, to eliminate any potential interference with crack propagation or stress concentrations caused by traces left by the milling tool, the impact face was polished with stone discs ranging from 50 to 6000 grit, resulting in a mirror-like finish. To mitigate any size effects on the results, the impact centers were positioned at least 5 cm away from the lateral free surface and from other impact locations.

2.3. Reference loading condition

Numerous dynamical indentation tests were performed on the aforementioned rocks. Although these tests considered impacts at various velocities, for the sake of clarity we will focus on and subsequently discuss the results of the igneous rocks for a single loading condition, as the main findings on these rocks could be supported just by analyzing one loading condition. This condition is regarded as the most representative of a DTH hammer in terms of energy, velocity, and the mass and length ratios between the piston and the bit, all of which have

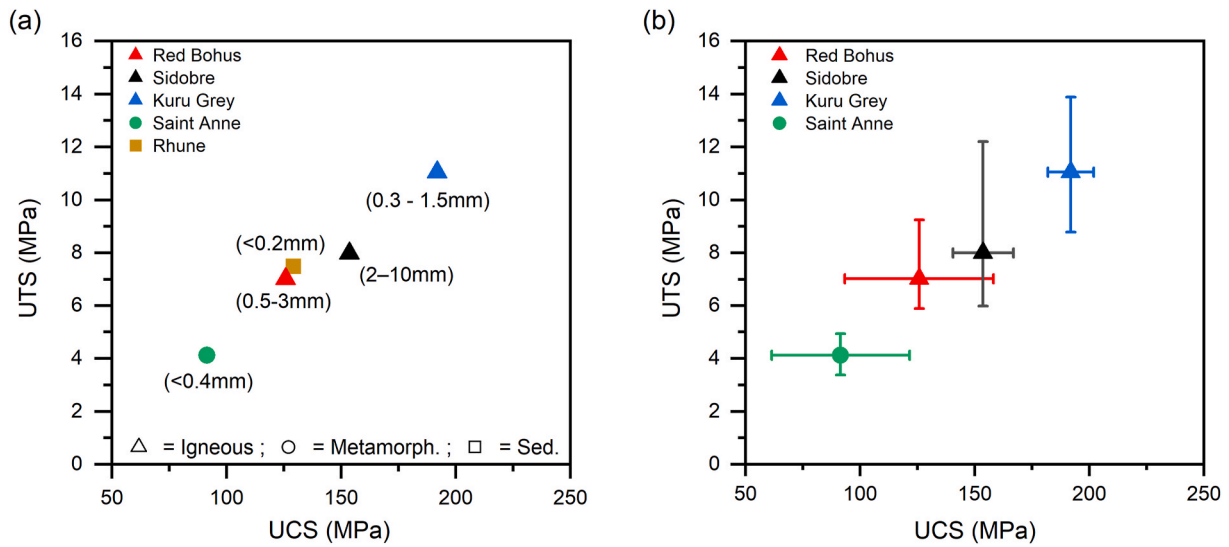


Fig. 2. (a) Average UCS and UTS for the set of rocks tested. The value in parentheses denotes the grain size. (b) Average and range of UTS and UCS when data were available.

been scaled to correspond to a single carbide insert bit. The specific values used were: Impact velocity $V_{pi} = 11$ m/s, WOB = 75 kg, piston length $L_p = 260$ mm, piston mass $m_p = 1.173$ kg, bit length $L_b = 272$ mm (including the carbide insert that protrudes 7 mm from the bit end), bit mass $m_b = 1.535$ kg, piston cross sectional area $A_p = 551$ mm², bit cross sectional area $A_b = 707$ mm². The tungsten carbide insert selected was a 16 mm spherical carbide insert as this size and shape is the most common in the frontal face of a DTH bit when drilling hard, abrasive rocks. Other loading conditions will be presented when required.

2.4. Indentation process and variables description

Fig. 3(a) shows the stress signal recorded at the center of the bit body. Just before the impact, the piston is moving towards the bit at a velocity V_{pi} . The impact creates an incident stress pulse that propagates through the bit with a time length given by $\tau = 2L_p/c$, and a stress magnitude given by $\sigma_i = (\rho c V_{pi}) Z_p / (Z_p + Z_b)$. When the pulse arrives at the strain gauges it sets the time origin $t = 0$. In theory, the incident pulse should have a rectangular shape; however, as explained by

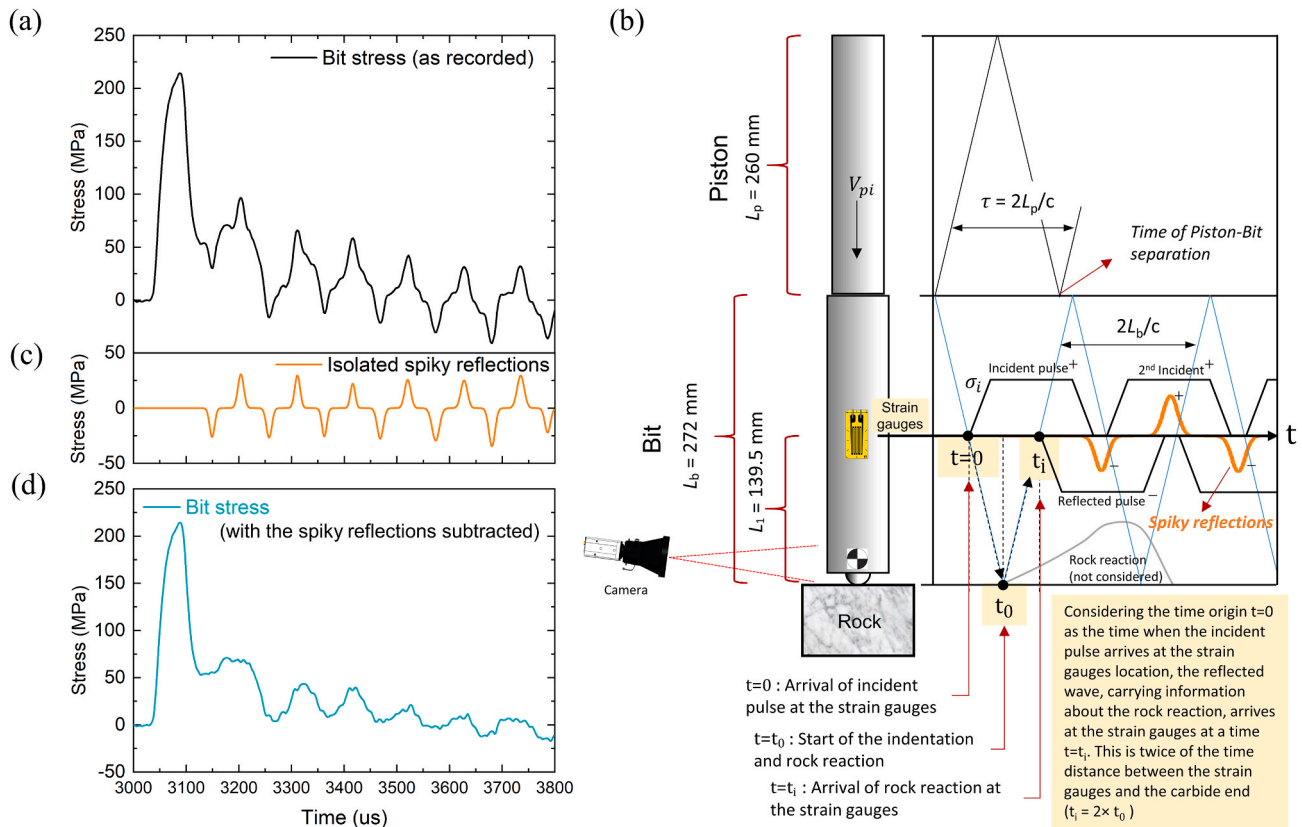


Fig. 3. (a) Bit stress signal as recorded by the strain gauges. (b) Lagrangian wave propagation diagram. (c) Isolated spiky reflections. (d) Bit stress signal with the spiky reflections subtracted.

Kaiser,⁴⁷ in Fig. 3(a) the incident pulse exhibits a softened profile due to the dispersive nature of longitudinal waves, the windowing effect of the strain gauge, and the gain bandwidth of the differential amplifier. In addition, there may be some angular and axial misalignments between the bit and the piston that could play a role in modifying the shape of the incident pulse.⁴⁸

When the front of the incident pulse arrives at the carbide end, the bit starts to penetrate the rock at a time $t_0 = L_1/c = 26.83 \mu\text{s}$, for $L_1 = 139.5 \text{ mm}$. Then, the compressive rock force reaction and the tensile reflected incident pulse starts to travel upwards towards the strain gauges. The arrival of the signal carrying information about the rock reaction to the strain gauges occurs at $t_i = 2L_1/c = 53.65 \mu\text{s}$, and coincides with the onset of the decay of the incident pulse. The timing definitions of $t = 0$, t_0 , and t_i , are also given in the Lagrangian wave diagram in Fig. 3(b). Spiky reflections with alternating sign resulting from the length mismatch between the piston and the bit can also be observed in Fig. 3(a). As deduced from the Lagrangian wave diagram, these fluctuations come from the multiple reflections of the incident pulse and their mutual self-cancellation. Since the time at which these small fluctuations occur can be known beforehand, they were isolated from the bit stress signal using the built-in Peak Fitting tool of Origin Pro, version 2023 (OriginLab Corporation, Northampton, MA, USA.). As a result, the isolated spiky fluctuations can be seen in Fig. 3(c). Subsequently, these were subtracted from the original signal. The stress signal in the bit without these spiky oscillations is shown in Fig. 3(d). For the sake of clarity, and in the interest of ease of identification of major changes in the stress signals in the following sections, hereafter, all the bit stress signals recorded at the position of the strain gauges will be presented with the spiky reflections subtracted. In addition, such derived stress signals will, for simplicity, be identified as bit stress signal.

Figs. 4 and 5 present the bit stress signals and typical piston and bit displacement curves for two distinct cases observed. These will be used to describe the indentation process. Firstly, Fig. 4(a) and (b) illustrate the case where re-contact between the piston and the bit was observed. Here, just before the impact, the piston is moving towards the bit at a velocity V_{pi} , thus carrying an energy $E_{pi} = 1/2 m_p V_{pi}^2$. As the indentation evolves, the bit attains its maximum indentation velocity V_{bi} before it completely slows down at the point of maximum indentation u_m , and the piston (lighter than the bit in these examples) rebounds at an instantaneous piston rebound velocity V_{pr} . The maximum stress σ_m in the bit stress signal—without considering the incident pulse—is registered at time t_p . As can be seen in Fig. 5(a), we emphasize that σ_m may not necessarily occur at the maximum indentation u_m . At t_{um} , the elastic recovery of the rock begins. If the rock has stored elastic energy, this

energy is subsequently given back to the bit in the form of kinetic energy, accelerating it up to a bit unloading velocity V_{br} . If V_{br} is high enough, the second contact between the piston and the bit will occur, as illustrated in Fig. 4(b). In this case, the bit exchanges its momentum with the piston, increasing the piston rebound velocity from V_{pr} to V'_{pr} . On the other hand, the bit decreases its velocity from V_{br} to V'_{br} . The occurrence of the re-contact can be observed in the bit stress signal as a second major stress pulse. The second pulse due to re-contact can be appreciated in Fig. 4(a).

The second case, illustrated in Fig. 5, represents the case where minimal elastic energy remains in the rock after the fragmentation. As shown in Fig. 5(b), in this case the second contact will never occur, and the final rebound velocity of the piston will be close to that predicted by the principle of conservation of momentum. This is because, during the time the impact faces are in contact, there are either no external forces acting, or their magnitudes are significantly smaller compared to the impact force itself. In addition, Fig. 5(b) shows how the WOB mechanism decelerates the bit, pushing it against the rock. Also note that in such cases the WOB does not act during most of the indentation, as the weight mechanism can not follow the extremely fast bit movement, primarily because of inertial differences given the ratios of forces/masses involved. For the two cases, the whole process ends at t_{end} once the bit re-contacts at a depth u_f the rock crater. This can be seen towards the end of the bit displacement curves in Figs. 4(b) and 5(b). Once u_f has been found, a horizontal projection is traced across the unloading curve. The time t_{uf} at which this line intersects the unloading curve defines the end of the first bit-rock interaction. Based on our analysis of a substantial number of videos, we can state that the second interaction between the bit and the rock is not capable of producing any more damage. However, if any fragments were previously created and not detached from the rock surface, they could be finally removed.

3. Data processing

In this section, we provide a comprehensive overview of the methodology used to correlate fracture events captured in the high-speed videos with their corresponding variations in both the bit stress signal and the displacement-time curve. Section 3.2 will present two detailed graphical examples, each chosen to represent distinct scenarios. These examples will introduce key features that characterize when fracture events occurred in the video footage. Also, a concise pictorial description of the evolution of the fracture is given. For our methodology, it is relevant that the origin of the displacement curve be accurately

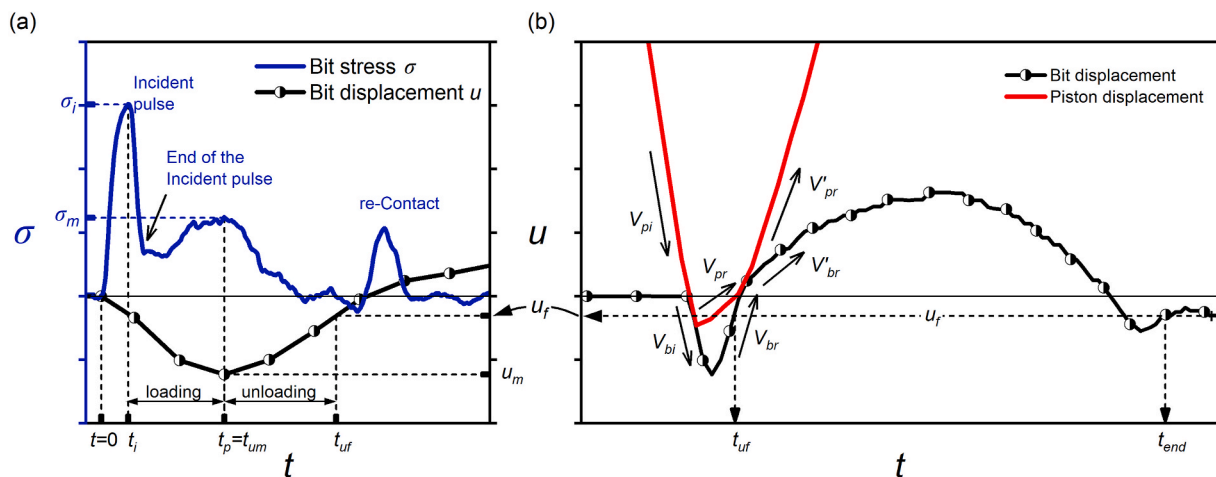


Fig. 4. Piston-bit-rock interaction: Case with re-contact between the bit and the piston. (a) Stress signal recorded at the center of the bit body (blue) and bit displacement from video tracking (black). (b) Displacement curves of the piston (red) and the bit (black). The vectors represent the velocities at different indentation stages. (For interpretation of the references to colour in this figure legend, the reader is referred to the Web version of this article.)

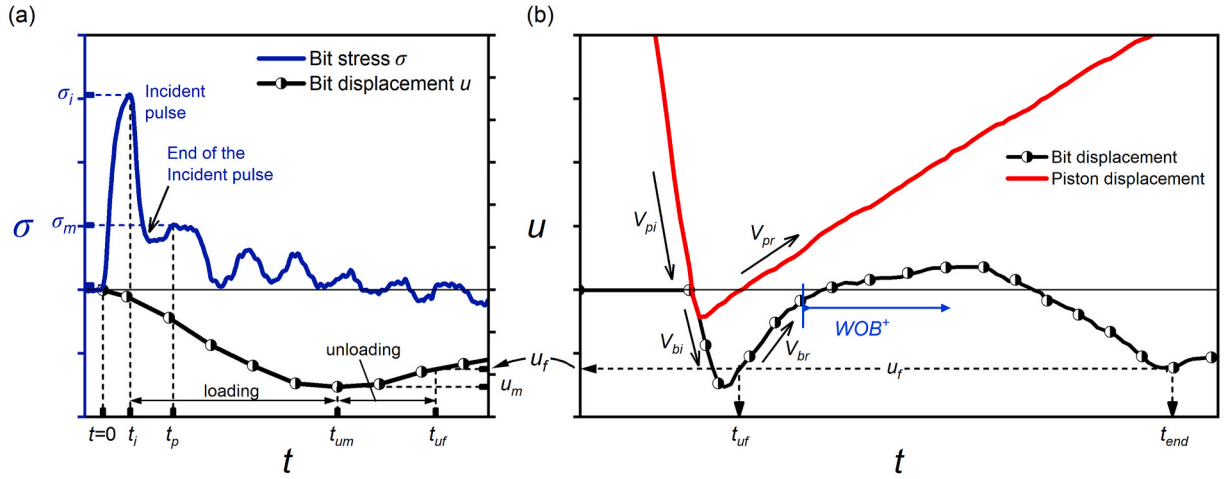


Fig. 5. Piston-bit-rock interaction: Case without re-contact between the bit and the piston. (a) Stress signal recorded at the center of the bit body (blue) and bit displacement from video tracking (black). (b) Displacement curves of the piston (red) and the bit (black). The vectors represent the average velocities at different indentation stages. The blue arrow points the beginning of the decline in bit velocity due to the sole action of the WOB. (For interpretation of the references to colour in this figure legend, the reader is referred to the Web version of this article.)

determined and match the origin of the bit stress signal. Since the bit indentation is derived from the video stream, a fracture detected in the video correlates in time directly with the displacement curve, but not with the strain gauges stress signal because the recording devices were not synchronized. The remaining challenge lies in harmonizing the time origin between the displacement curve and the bit stress curve. The following section addresses this problem and proposes effective solutions to ensure accurate alignment and correlation.

3.1. Curves origin synchronization

As the time step achievable with the high-speed camera is not low enough to precisely determine the beginning of the indentation, we define a procedure to align the displacement curve with the time origin of the bit stress signal. This alignment is achieved using the following approach:

By implementing the piston-bit-rock second-order model described in Song et al.,² while considering the key distinction that in our setup A_p

and A_b are not equal (thus, the amplitude of σ_i is a function of the mechanical impedances), this model can be reformulated as follows:

$$\ddot{u} + \left(\frac{\rho c A_b}{m_b}\right) \dot{u} + \left(\frac{k}{m_b}\right) u = \left(\frac{2A_b}{m_b}\right) \sigma_i \quad (1)$$

$$\sigma_i = \begin{cases} (\rho c V_{pi}) Z_p / (Z_p + Z_b), & t \leq \tau \\ 0, & t > \tau \end{cases} \quad (2)$$

Running the model for a wide range of k apparent rock stiffness, ranging from a very soft $k = 5 \times 10^5$ N/m to a very hard $k = 7.5 \times 10^8$ N/m, and using the parameters of our setup listed in section 2.3, we were able to simulate the bit displacement u over time. All the displacement curves for an impact velocity V_{pi} equal to 11 m/s are plotted in Fig. 6(a). We observed that, for time interval less than 50 μ s, the bit displacement u exhibits nearly identical values across all the apparent rock stiffness values, and that any discrepancies whether in terms of time or displacement, are negligible within the overall time scale of the entire process and the scope of our analysis. This observation allows us to

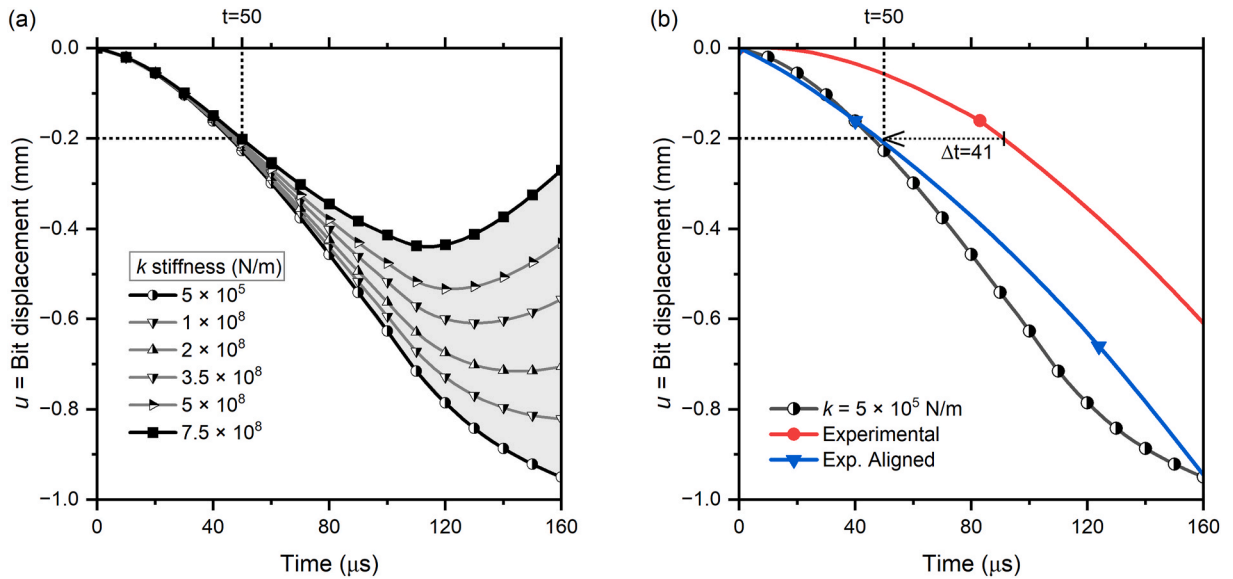


Fig. 6. (a) Simulated bit displacement curves against time for a wide range of feasible k apparent rock stiffness. (b) Experimental curve (red) shifted 41 μ s to the left (blue) to align with the point (50 μ s, -0.2 mm). (For interpretation of the references to colour in this figure legend, the reader is referred to the Web version of this article.)

define that the experimental displacement curve of the bit —when the impact velocity is 11 m/s— has to pass over the point $t = 50 \mu\text{s}$ and $u = 0.2 \text{ mm}$. Similar points can be found at different impact velocities. Once the experimental curve has been found, we adjust it accordingly. Fig. 6 (b) depicts the original displacement curve (red) and the corresponding adjusted curve (blue) aligned with the point $(50 \mu\text{s}, -0.2 \text{ mm})$. As the model is zero-dimensional, the displacement u should be taken as the displacement of the center of bit mass. As the strain gauges were located at the center of the bit mass, both time origins perfectly match.

3.2. Correlating fracture events with the bit stress signal

To properly describe the procedure employed, two time parameters must be defined.

t_1 : Time (from video) at which radial cracks were first observed on the rock surface.

t_2 : Time (from video) at which large fragments were first observed to form on the rock surface.

Using this notation, it will be easy to later discriminate when a fracture event occurs during loading or during unloading, as when $(t_2 - t_0)/(t_{um} - t_0) \leq 1$ chipping occurs during the loading stage, meanwhile for $(t_2 - t_0)/(t_{um} - t_0) > 1$ chipping occurs in the unloading. The subtraction of t_0 in the ratio accounts for the delay t_0 between the center of bit mass and the end of the carbide insert. We emphasize here that both t_1 and t_2 are not the time at which each type of crack was created, but when they first can be observed in the high-speed videos. Fig. 7 schematically represents a simplified evolution of a fragmentation process as described in G. Wu et al.⁷ In this representation, we exclusively focus on radial and side cracks, disregarding other crack types. At $t = t_0$ the incident pulse reaches the carbide insert end, which was held in contact with the rock due to the action of the WOB. The carbide insert begins to penetrate the rock, initiating the generation of a highly stressed and plastically deformed zone beneath the indenter. From this zone, a network of cracks will propagate later. By $t = t_1$, radial cracks propagate from the center of the indentation due to hoop-stresses and are visible on the rock surface. Simultaneously, side cracks propagate under and almost parallel to the surface and remain imperceptible from above (they are visible in the cross-view section). Finally, at $t = t_2$, radial cracks continue to extend outward from the center and side cracks emerge, leading to the formation of large fragments that can be eventually detached from the rock.

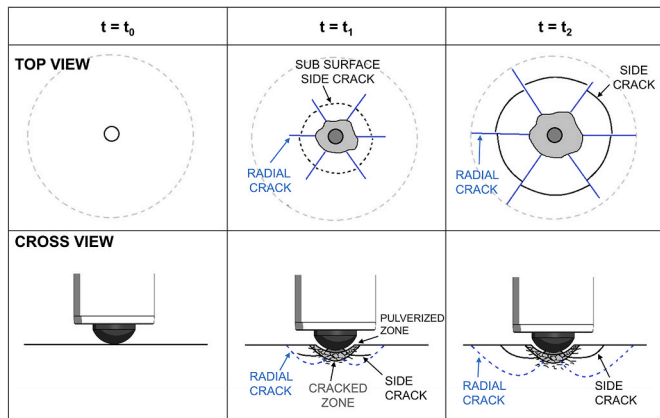


Fig. 7. Schematically indentation evolution of a fracture network at time $t = t_0$ (bit initial position and beginning of the indentation), $t = t_1$ (radial cracks observation), and $t = t_2$ (side cracks observation). Upper row correspond to the rock top view. Bottom row correspond to a cross sectional view.

3.2.1. Example I: Saint Anne limestone

Fig. 8(a) shows an indentation process in the Saint Anne limestone in which the maximum stress σ_m occurs before the maximum indentation u_m , and Fig. 8(b) shows a frame-by-frame pictures of the video footage. Arrows were drawn pointing to specific fragmentation features, like radial cracks or chipping contours, when their appearance were first noticed on the rock surface. The frame corresponding to the end of the fragmentation and the crater image, after debris cleaning, are provided in Fig. 8(c) and (d), respectively. In the last frame, we slightly remarked the crater contour. The frame numbers are also displayed in the displacement curve using a numeral sign. The piston impact velocity V_{pi} was 10.66 m/s and the bit-rock interaction curve is representative of all the impacts performed on the Saint Anne limestone. The maximum displacement u_m occurs at frame # 3, so in between frame # 0 and frame # 3 the bit experiences the loading phase, meanwhile from frame # 3 and beyond, the bit experiences the unloading phase. At frame # 2, a small radial crack propagates to the left, setting $t_1 = 167 \mu\text{s}$. This fracture releases some accumulated strain. Consequently, this have to prevents further increase of the stress, and a change in the slope of the bit stress signal is expected. We identified two major slope changes at $t = 182 \mu\text{s}$ and $t = 273 \mu\text{s}$, as can be seen in Fig. 8(a). To determine which of the two major slope changes corresponds to t_p or t_r , we examine the corresponding stress values. First, the stress value of the slope change from which the bit stress decays to zero is examine. If the corresponding stress value also coincide with the maximum stress σ_m , then this slope change is set as t_p . Using the observation that a radial crack always occurs earlier than the side cracks, the first slope change is set as t_r . In this case, it is obvious from the definition of t_p that $\sigma_r \leq \sigma_m$. On the other hand, in the case the stress magnitude related to the earlier slope change results greater than the stress of the lately slope change closer to the stress drop, t_r is set equal to the time of the earlier slope change. According to the definition of t_p , it also applies in this case that $t_p = t_r$. Finally, in the case a single major slope change is identified earlier than the first stress drop, this slope change is set as t_p and t_r is left undefined. According to this description, the first slope change in Fig. 8(a) coincides with t_p and, at the same time, with t_r . At frame # 3 the bit reaches its maximum displacement, setting $t_{um} = 250 \mu\text{s}$. As no fragmentation has been observed yet, the major drop in the stress signal occurred mainly due to the beginning of the unloading phase and the ongoing propagation of cracks, that as can be observed in frame # 3 and # 4 of Fig. 8(b),

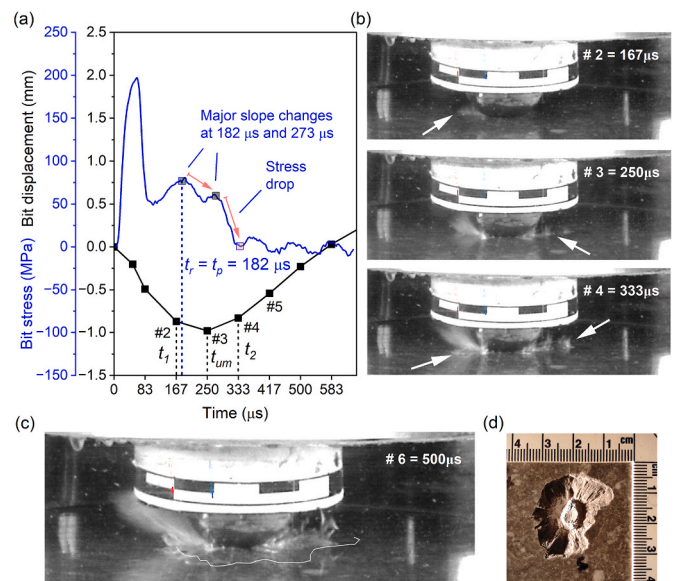


Fig. 8. (a) Bit stress signal and displacement versus time for Saint Anne limestone. (b) Frame by frame indentation pictures. (c) Frame time at which the crater is completely defined (500 μs). (d) Crater.

mainly correspond to radial cracks. In frame # 4, during the unloading stage, some fragments detaching from the rock were observed, becoming increasingly evident as they progress to frame # 6. The observation of fragments at frame # 4 sets $t_2 = 333 \mu\text{s}$.

3.2.2. Example II: sidobre granodiorite

Fig. 9(a) shows an indentation process in the Sidobre granodiorite in which big fragments formation occurs before the bit reaches the maximum indentation depth. This was often observed in the tests performed with the igneous rocks. Frame # 1 in Fig. 9(b) shows a small radial crack propagating to the left, setting $t_1 = 73 \mu\text{s}$. In frame # 2 a big fragment detaching from the surface can be observed, which sets $t_2 = 164 \mu\text{s}$. According to the description provided in preceding section, only the slope changes in the bit stress signal that occurs earlier than the stress drop have to be considered. This leads to the identification of a single major slope change at $t = 175 \mu\text{s}$, setting $t_p = 175 \mu\text{s}$ and an indeterminate value for t_r . As the radial crack was created prior to the end of the incident pulse, it was not possible to gather information about this event from the bit stress signal, been this the ultimate reason for the indetermination of t_r . Results interestingly to note that the maximum stress t_p was found slightly later than t_2 because the fragment was created between frame # 1 and frame # 2. The high-stress reflections coming like from a free end boundary observed from time frame # 3 and

beyond —at a frequency multiple of the time length of the bit $2L_b/c = 105 \mu\text{s}$ — is evidence that the tip of the carbide momentarily lost the support of the rock. We emphasize that the stress relief was due to the creation of fragments, and not the other way around. Due to inertial effects, the bit continues moving downwards, but no more damage was visible. Finally, at frame # 4 the unloading process initiates, setting $t_{um} = 346 \mu\text{s}$. The frame at which the crater is completely defined is shown in Fig. 9(c), and a picture of the crater is provided in Fig. 9(d).

4. Results and analysis

4.1. Crater shape

Fig. 10 shows the craters of the five rocks impacted in this study under the reference condition described in section 2.3. In the igneous rocks, the cratering was extensive and not symmetrical, with a plurality of radial cracks of different lengths. The zone under the insert was disintegrated and ejected during the indentation due to a brittle behavior. In contrast, in the Saint Anne limestone and the Rhune sandstone, the radial cracks tend to be more uniform, and the zone under the insert was not pulverized, but plastically deformed. In limestone, fragments were produced from under and the sides of the re-compacted zone, while in sandstone, which was the rock with the highest porosity, only a permanent protrusion or “pile-up” was obtained. This characteristic was

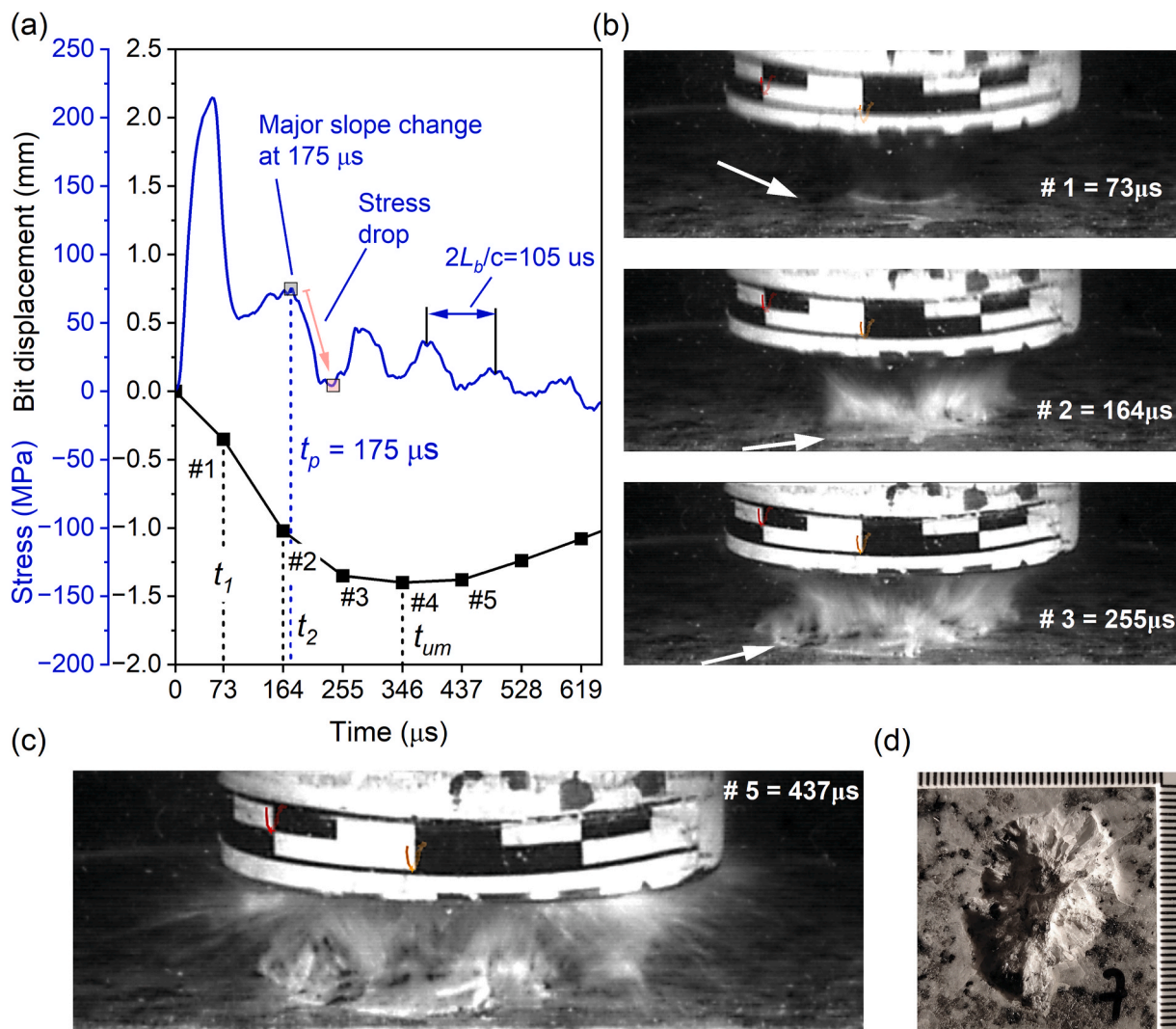


Fig. 9. (a) Bit stress signal and displacement versus time for Sidobre granodiorite. (b) Frame by frame indentation pictures. (c) Frame time at which the crater is completely defined ($500 \mu\text{s}$). (d) Crater.

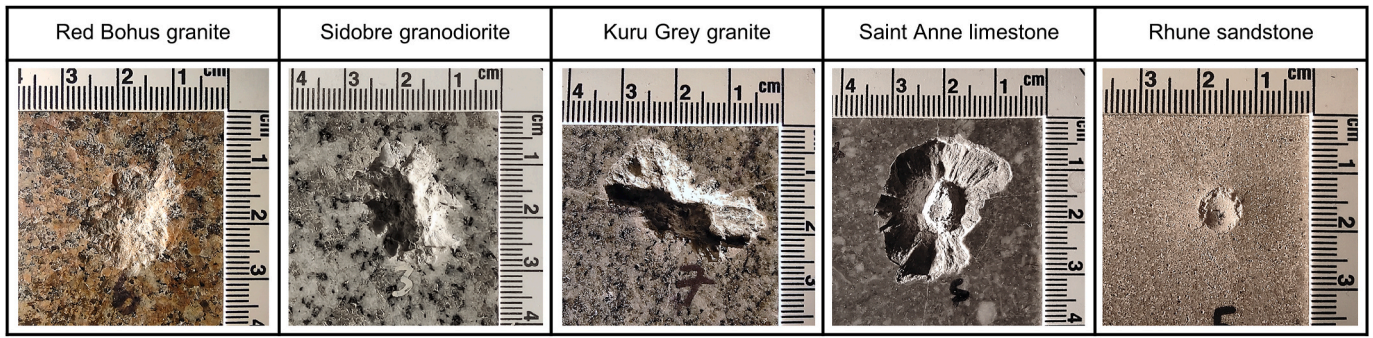


Fig. 10. Different crater shapes impacted at the reference loading condition. Impact energy = 75 J, piston velocity = 11 m/s, 16 mm spherical carbide insert.

preserved even at other tested velocities. It is believed that the preservation of the re-compacted zone is the reason for a high bit rebound velocity and a re-contact in limestone and sandstone, as the tip of the carbide never loses contact with the rock, and any elastic recovery of the rock is given back to the bit.

4.2. Stage in the fragmentation process at which side cracks are created

As pointed out in the introduction, the focus has been on whether side cracks form during loading or unloading processes. Particularly, the time at which fracture events occur is extremely important when the indentation process has to be characterized because these events induce changes in the bit stress signal. Accurately identifying which type of crack has produced a change in the stress signal within the bit would help calibrating simulations that accurately predict the occurrence of radial or side cracks in various rock types. So far, several authors who have generated dynamic curves have noted these changes as fragmentation, fluctuations, or chipping events, without specifying the nature of the crack type responsible for such changes.^{19,23,25,30,44,45}

Because each test has been video recorded, we have been able to identify and correlate with the stress signal the effect that the onset of a radial or side crack produces in some particular rocks. Discerning between both without the aid of a high-speed camera is an impossible task when side cracks that generate large fragments occur during unloading, since in such cases, there is no rock-related information in the stress signal because the bit has already lost contact with the rock surface. In contrast, as radial cracks always occur during or at most at the end of the loading phase, there is always information about them in the stress signal of the bit. However, depending on the time of their occurrence,

their information may be obscured by the superposition of reflections.

In the following, we will describe three typical cases found in relation to the instant at which radial cracks (t_1) and side cracks (t_2) appear in relation to the maximum indentation time (t_{um}), and the relation those times have with changes in the slope of the bit stress signal. We consider these three cases because whatever the rock tested is, the bit stress/indentation curves can be classified in one of these three cases, as a kind of stress signature. Fig. 11 shows these three cases. The generality of this classification is useful to work with bit stress curves that can be very dissimilar. It is worth noting that Saadati et al.¹⁰ also arrived to a three general rock indentation response, but focusing more on the force level required to fragment the rocks, rather than the stage at which fragmentation occurs.

Case 1. The peak of the stress in the bit at t_p nearly coincides with the observation of a fragment created during the loading stage by a side crack at t_2 , being $t_2 < t_{um}$. Radial cracks at t_1 occur early than t_p .

Case 2. The observation of a radial crack at t_1 nearly coincides with a change of the slope of the bit stress signal that defines the peak of the stress in the bit at t_p , being $t_p < t_{um}$. Fragmentation due to side cracks is observed during the unloading stage, with $t_2 \geq t_{um}$.

Case 3. Radial cracks appear at t_1 and are close to a slight stress relief in the bit at t_r . As the indentation continues, the stress in the bit increases until a maximum at t_p , with $t_p \approx t_{um}$. The rock fragmentation due to side cracks occurs during the unloading stage at $t_2 \geq t_{um}$.

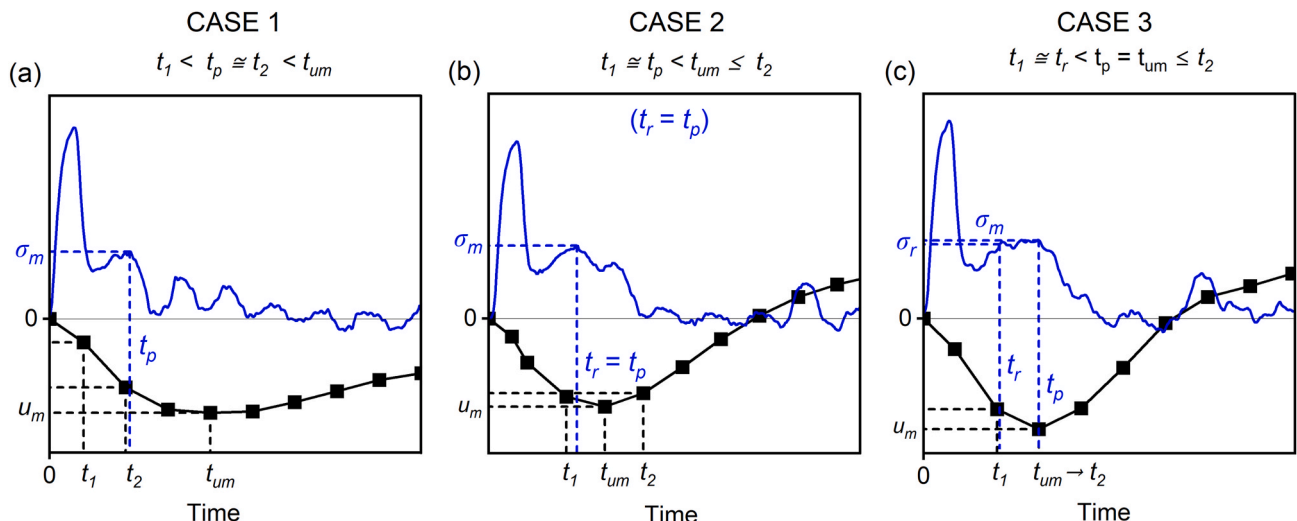


Fig. 11. Typical cases to represent the onset of radial and side cracks in relation to t_p and t_{um} . t_1 = onset of radial cracks, t_2 = onset of side cracks.

4.3. Igneous results

The inherent heterogeneity of the igneous rocks²⁴ produced significant variations in the bit stress curves under identical loading conditions. This can be explained by the large dispersion in crater volumes. To provide reliable results, we subjected each rock sample to eight impacts, at distinct locations spaced at least 5 cm from the center of neighbouring craters or surrounding radial cracks. Out of the eight impacts performed, six were focused on the bit end and the rock, while two (typically impact # 4 and impact # 8) were focused on the interaction between the piston and the impact face of the bit. This explains the blank data in Table 1, as no information on the timing of the chipping could be determined. Rather than becoming a problem, the dispersion obtained was used to explain some aspects related to the efficiency of the indentation and, to a certain extent, illustrate the probabilistic nature of the fragmentation process in these rocks. Fig. 12(a)–(k) show the bit stress responses of Red Bohus granite, Sidobre granodiorite, and Kuru Grey granite. The figures are sorted in rows accordingly time t_p . In these figures, the number following the rock name identifies the rock sample, while the number after the hyphen indicates the sequence of the impact on that sample. Some similarities can be observed in the curves, even when they are not related to the same rock type. According to the preceding section, most of these curves can be classified as CASE 1, except curves (a) and (b) which fall into a classification CASE 3. Table 1 presents the relevant results for these rocks at the reference loading condition described in section 2.3. The Specific Energy (SE) presented in the last column of Table 1 was calculated as the ratio of the piston impact energy to the crater volume. In Fig. 13(a) the ratio $(t_2 - t_0)/(t_{um} - t_0)$ was plotted. As can be seen, in the igneous rocks, most of the side cracks occur during the loading or at most at the end (ratio ≤ 1). Fig. 13(b) shows the correlation existing between t_2 and t_p , meaning the detection of fragments in the videos is the cause of the abrupt stress drop detected at t_p .

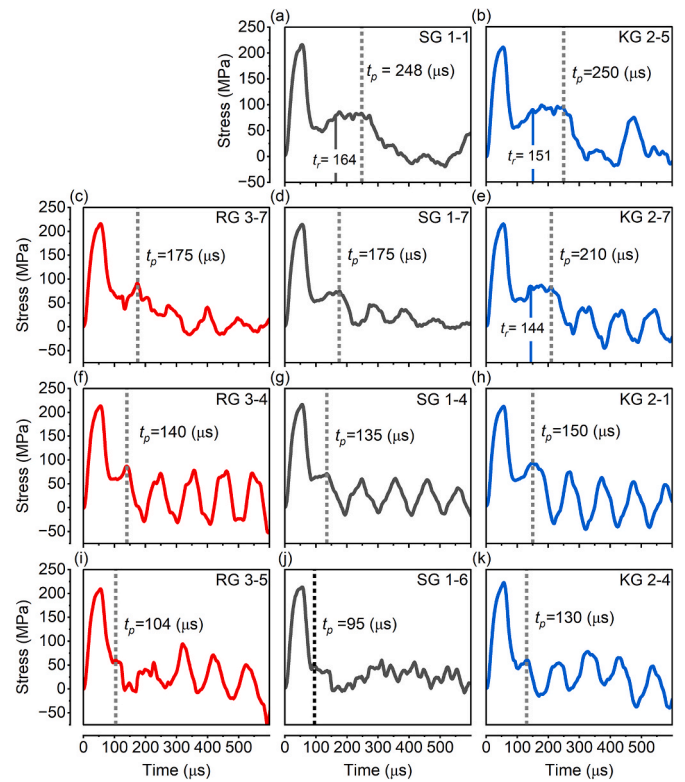


Fig. 12. Bit stress time curves sorted according the time t_p . First column: Red Bohus granite. Second column: Sidobre granodiorite. Third column: Kuru Grey granite. (a) and (b): stress signature CASE 3. (c) to (k): stress signature CASE 1. (For interpretation of the references to colour in this figure legend, the reader is referred to the Web version of this article.)

Table 1

Relevant results for igneous rocks impacted at the reference condition.

Rock	Test #	Impact vel (m/s)	Rebound vel (m/s)	WOB (kg)	u_m^a (mm)	t_{um}^a (μs)	t_2^a (μs)	t_1^a (μs)	$t_2^b/t_{um}^{a,d}$ (s/s)	t_r^b (μs)	t_p^c (μs)	SE (MJ/m ³)
RG	3-1	11.0	0.8	76.3	1.86	455	91	91	0.15		132	229.9
	3-2	11.1	0.8	80.8	1.97	455	91	91	0.15		120	153.8
	3-3	11.1	0.7	79.9	2.17	530	167	167	0.28		147	241.4
	3-4	11.1	1.1	78.1							140	193.1
	3-5	11.2	0.5	78.0	1.61	425	61	61	0.09		104	566.0
	3-6	11.2	0.7	76.2	1.18	339	157	66	0.42		177	268.7
	3-7	11.1	1.0	79.7	1.05	273	182	91	0.63		175	150.4
	3-8	11.2	1.2	79.3							125	358.7
SG	1-1	11.1	3.7	75.7	1.09	263	263	81	1.00	164	248	127.1
	1-2	11.2	0.5	78.3	1.91	540	177	86	0.29		135	242.4
	1-3	11.2	0.9	77.2	2.31	584	130	130	0.19		135	219.2
	1-4	11.2	0.9	76.7							135	238.5
	1-5	11.2	1.0	77.7	1.72	395	122	122	0.26			309.2
	1-6	11.1	2.3	76.5	1.68	354	81	81	0.17		95	426.0
	1-7	11.1	0.5	78.4	1.42	346	164	73	0.43		175	140.4
	1-8	11.1	1.0	79.1							100	256.2
KG	2-1	11.0	1.0	79.2	1.35	455	182	91	0.36		150	266.2
	2-2	11.1	0.9	78.3	1.51	455	182	91	0.36		145	274.3
	2-3	11.1	0.9	78.2	1.83	566	112	112	0.16		145	242.1
	2-4	11.0	1.0	78.7							130	360.5
	2-5	11.0	5.3	79.3	0.94	218	218	127	1.00	151	250	258.1
	2-6	11.0	4.5	79.8	0.98	222	222	131	1.00	156	250	211.7
	2-7	11.0	0.9	79.0	1.12	227	227	136	1.00	144	210	190.0
	2-8	11.0	1.0	79.0							190	204.4

Notes.

^a Blank data due to no video recordings.

^b Blank data means t_r was non detectable in the stress signal.

^c Blank data due to the stress signal was partially recorded.

^d $t_2^b = t_2 - t_0$; $t_{um}^b = t_{um} - t_0$.

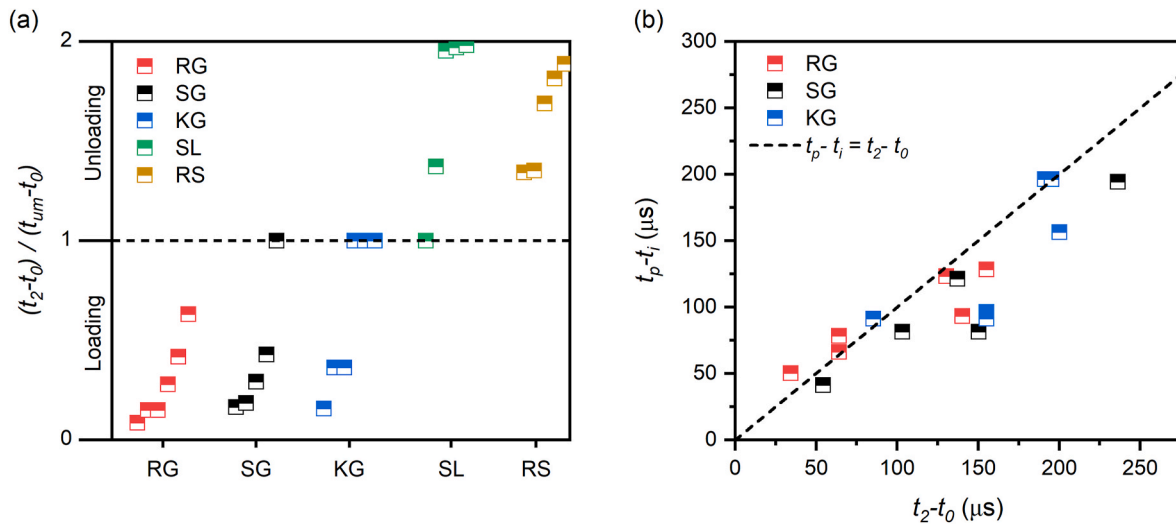


Fig. 13. (a) Time ratio $(t_2 - t_0) / (t_{UM} - t_0)$ for the set of rocks tested. A ratio bigger than 1 means that chipping was observed during the unloading of the bit, meanwhile a ratio smaller than 1 means that chipping was observed during the loading stage. (b) Correlation between t_2 (detection of side cracks in videos) with t_p (time at which the peak stress occurs).

4.4. Limestone and sandstone results

Fig. 14(a) shows the stress curves for the Rhune sandstone for impact velocities ranging from 8.71 m/s to 14.0 m/s. Only the cases in which fragmentation was obtained and for those the Specific Energy (SE) could be calculated were included in Table 2. Interestingly, this rock needed a higher impact velocity than the Kuru Grey granite for chipping, even if from the point of view of their mechanical properties, the sandstone is considered a less competent rock. This rock can be classified according to section 4.2 as a rock with stress signature CASE 3, given the maximum stress time t_p coincides with the maximum indentation t_{UM} , and the slope change at t_r coincides with t_1 . The fragmentation time t_2 occurred during the unloading stage at times ranging from 382 μs to 436 μs . Fig. 14(b) shows the original bit stress curves without the subtraction of the spiky reflections obtained from rock samples subjected to testing at 11 m/s. Notably, the five curves look almost identical. This empirical evidence underlines the high reliability and repeatability of our system, suggesting that the variations observed in the igneous rocks can be attributed solely to the bit-rock interaction, excluding any unwanted interactions with the setup or the recording devices.

Fig. 14(c) shows the stress curves recorded from impacts on Saint Anne limestone samples. As expected, the shape of the bit stress signals is scaled by a factor proportional to the impact velocity, further validating the reliability of the results. In this rock, the stress signature aligns with the CASE 2 classification. It is interesting to note that t_r (equal to t_p in this rock) was not constant as in the case of Rhune sandstone, as it has a small tendency to occur early as the impact velocity is increased. For example, taking into consideration the results of the tests SL 2-1 and SL 5-4 provided in Table 2, at an impact velocity equal to 6.2 m/s t_r occurs at 208 μs , meanwhile at an impact velocity equal to 11.8 m/s, t_r occurs at 182 μs . Moreover, the time at which the re-contact occurs was not constant, as opposed to the Rhune sandstone, in which the time of the re-contact occurs always at the same time, approximately at 600 μs . The chipping in this rock occurred also during the unloading at t_2 times between 250 μs and 392 μs . Fig. 14(d) shows the correlation existing between t_1 and t_r . Aside the red marker enclosed in a circle that falls away from the trend, the correlation is remarkable. This correlation suggests that the detection of radial cracks in the videos is the root cause of the slight change of slopes detected at t_r .

4.5. Side cracks and indentation efficiency

A widely used metric to quantify the indentation efficiency is by using the Specific Energy, SE [J/m^3], the energy expended to produce a unit volume of fragments.⁴⁹ As pointed out in the introduction, the literature related to this topic states that side cracks have a major influence on the efficiency of the indentation process,^{21,37,50,51} and that SE can be correlated with DTH penetration rates.⁵²⁻⁵⁶ Most of these claims regarding side cracks have primarily originated from simulations, without dynamical experimental evidence to substantiate them. Hereinafter, we provide a plausible explanation linked to the experimental evidence. By plotting SE of every impact listed in Table 1 against t_2 , a clear correlation emerges: The earlier the stress drop occurs, the higher is the specific energy. See Fig. 15. It's important to reiterate that t_2 is intrinsically correlated to the time at which side cracks are created inside the rock. A feasible explanation for the dispersion can be that this is due to the existence of small flaws or weaknesses randomly distributed in the volume of the rock,^{41,57} and a similar random behavior in the force-penetration curves of an Inada granite was observed by Hashiba et al.⁴⁴ The activation of these flaws can occur at different times, depending on their depth and size, thereby altering the trajectory that side cracks must follow to reach the surface. If the activated flaw lies closer to the surface, the path to travel to the surface has to be shorter, in contrast to a flaw activated at greater depth. Consequently, with constant crack propagation speed, the emergence of a side crack on the surface is detected earlier (t_2). Furthermore, the size of the generated fragment has to be smaller if the side crack originated from a flaw closer to the surface (thus SE is high), or larger if it originates from a deeper flaw (thus SE is small), explaining the correlation found between the specific energy and t_2 .

5. Conclusions

This paper presents the results of dynamic impact studies on different rock types, contributing to a better understanding of the indentation process. A new experimental setup was built that fairly replicates the mechanical characteristics and the loading conditions of a DTH hammer. This setup allows us to derive piston and bit indentation curves by tracking their position using high-speed video recordings, enabling a closer examination of bit/rock interaction and the evolution of the fragmentation process. For the tested piston/bit mass and length relationship, the rebound velocity of the piston immediately after the impact

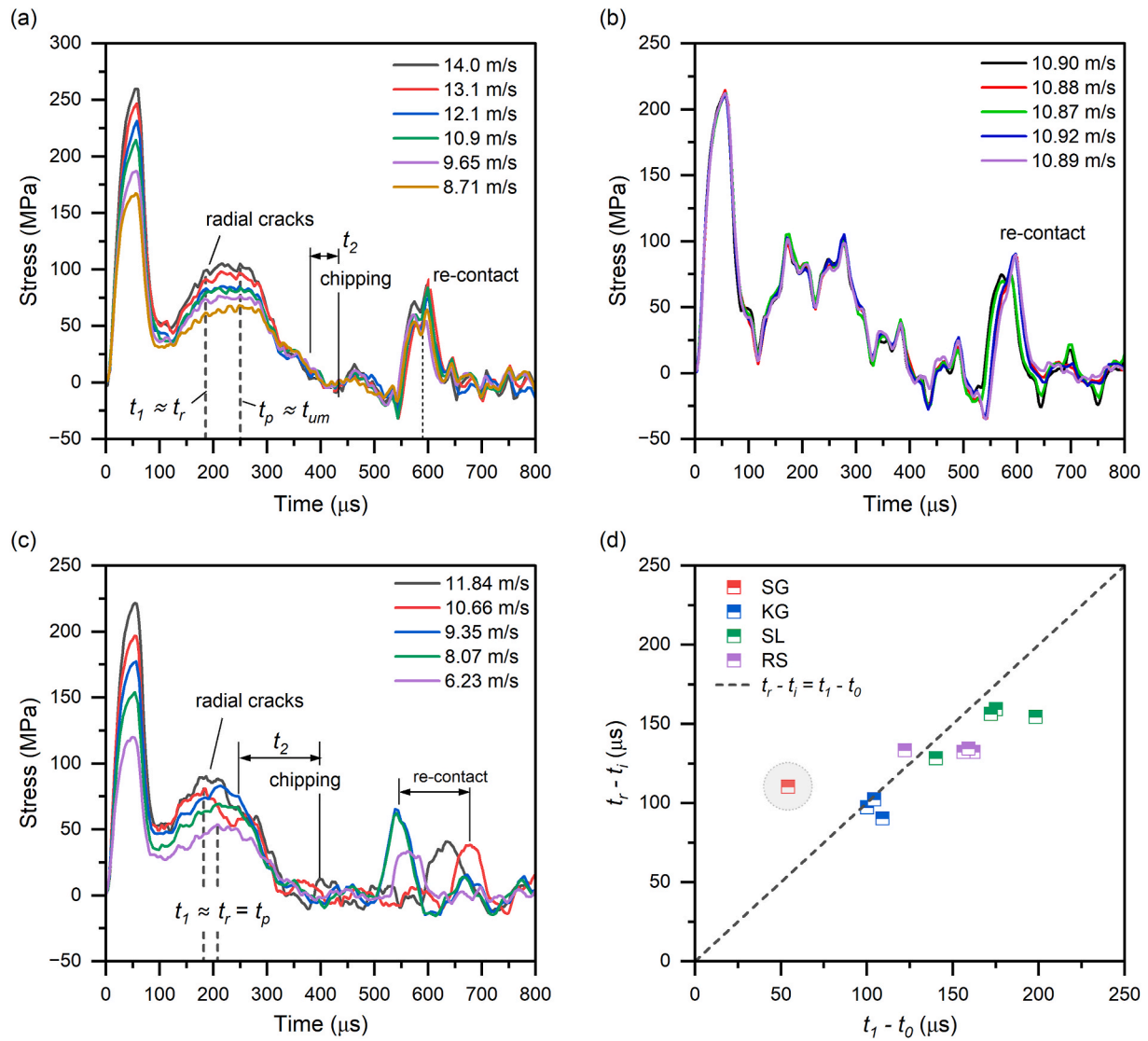


Fig. 14. (a) Bit stress curves for Rhune sandstone tests, classified as signature CASE 3. (b) Five bit stress curves as recorded for Rhune sandstone impacted at 11 m/s. (c) Bit stress curve for Saint Anne limestone tests, classified as stress signature CASE 2. (d) Correlation between the time t_1 at which radial cracks were observed against the time t_r at which the stress signal showed a change in the slope.

Table 2
Impact conditions and relevant measurements for Saint Anne limestone and Rhune sandstone.

Rock	Test #	Impact vel (m/s)	Rebound vel (m/s)	WOB (kg)	u_m (mm)	t_{um} (μ s)	t_2 (μ s)	t_1^a (μ s)	t_2^b/t_{um}^b (s/s)	t_r (μ s)	t_p (μ s)	SE (MJ/m ³)
SL	2-1	6.2	3.0	26.2	0.68	190	392	225	2.24	208	208	97.7
	3-1	9.4	4.1	25.6	0.86	202	369	202	1.95	213	213	123.8
	3-3	8.1	3.7	25.7	0.73	199	366	199	1.97	210	210	559.1
	5-4	11.8	4.0	21.9	0.99	250	250	167	1.00	182	182	148.3
	6-5	10.7	3.3	22.2	0.98	250	333	167	1.37	182	182	194.6
RS	2-1	13.1	5.6	75.8	1.33	215	382	189	1.89	187	250	197.8
	2-2	14.0	6.0	73.9	1.41	272	356	189	1.34	186	250	177.6
	2-3	13.9	5.9	74.2	1.43	266	350	183	1.35	186	250	224.3
	2-4	13.1	5.6	77.8	1.40	232	399	149	1.81	187	250	426.7
	2-6	12.1	5.1	75.3	1.23	269	436	186	1.69	188	250	448.8

Notes.
^a Blank data as no radial crack could be observed.
^b $t_2^b = t_2 - t_0$; $t_{um}^b = t_{um} - t_0$.

remains almost constant, consistent with the law of conservation of momentum in one dimension. When the piston rebound velocity is higher than the predicted by the law of conservation of momentum, this is attributed to a re-contact between the bit and the piston during the

unloading stage of the bit. This phenomenon predominantly occurred in the tested sandstone and limestone, with infrequent occurrences in the igneous rocks. This divergence in behavior within igneous rocks highlights a distinct rock response, where the zone beneath the carbide insert

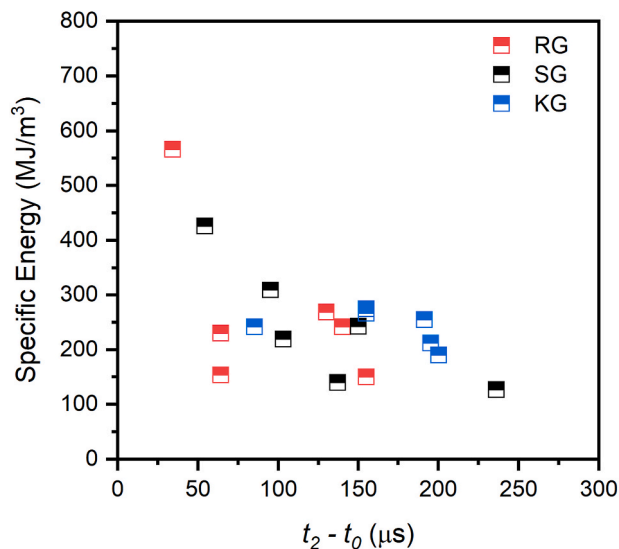


Fig. 15. Relationship between Specific Energy and t_2 .

is pulverized and ejected, in contrast to sandstone and limestone, where the plastically deformed zone beneath the inserts remains intact after the indentation. Furthermore, this study revealed correlations between fragmentation events, changes in the stress-time curves of the bit, and bit loading and unloading curves. The conclusions can be summarized as follows:

The time at which side cracks occur in relation to the maximum indentation is dependent on the rock type. In the tested igneous rocks, all rock damage occurs during the loading phase of the bit, with radial and side cracks appearing either before or at the point of maximum bit indentation. The damage in igneous rocks is directly correlated to the early or late formation of the side cracks during the loading movement of the bit, reinforcing the notion that the presence of side cracks significantly influences the indentation efficiency. The dispersion in the SE highlights that the process of fragmentation is intrinsically more probabilistic than deterministic, likely attributable to the inherent randomness in the distribution of flaws and weaknesses within the rock samples.

In limestone and sandstone, under the specific loading conditions tested, side cracks occurred always during the unloading phase of the bit. While in sandstone the radial cracks always emerged at the same time, in limestone, the radial cracks tended to form early as the impact velocity systematically increased.

The similarities in rock responses allowed us to establish three distinct stress signature responses based on major fracture events relative to the maximum indentation. These signature responses provide a valuable framework for classifying different rocks reactions to dynamic indentations, challenging the idea that a single behavior can describe the response behavior of rocks, thus calling into question previously postulated assumptions. The long-established argument in the literature that side cracks can occur in the loading stage solely due to boundary conditions or misinterpretation of side cracks does not hold, as boundary conditions would affect weaker rocks more significantly. Our findings demonstrate that fragmentation can persist during unloading for some rocks less competent than the igneous rock tested. Hence, the observed behavior appears to be more influenced by the loading conditions, rock fabric, internal defects, and mechanical properties, rather than rock boundary conditions.

Determining the specific factors that promoted these different behaviors was beyond the scope of this study. Nevertheless, it is believed that further exploration using numerical simulations, incorporating rock heterogeneity (e.g. variation in grain minerals size and strength) and initial rock states (e.g. probabilistic flaw distributions) will be

instrumental in revealing the underlying mechanisms. Additionally, testing different loading conditions and insert shapes may shed light on whether these observations are intrinsically related to rock properties or not.

Funding

This work is part of a PhD funded by Drillco Tools S.A. and Mines Paris PSL.

CRedit authorship contribution statement

Jorge Aising: Writing – original draft, Visualization, Validation, Methodology, Investigation, Formal analysis, Conceptualization. **Laurent Gerbaud:** Writing – review & editing, Supervision, Methodology. **Hedi Sellami:** Writing – review & editing, Supervision, Methodology.

Declaration of competing interest

The authors declare the following financial interests/personal relationships which may be considered as potential competing interests: Jorge Aising reports financial support was provided by Drillco Tools S.A. Jorge Aising reports a relationship with Drillco Tools S.A. that includes: employment. If there are other authors, they declare that they have no known competing financial interests or personal relationships that could have appeared to influence the work reported in this paper.

Data availability

The data that has been used is confidential.

Acknowledgements

The financial support provided by Drillco Tools S. A. is gratefully acknowledged. We also acknowledge the support of Armines for the help in the preparation of the rock samples and the commissioning of the experimental setup.

References

- Chiang LE, Stamm EB. Design optimization of valveless DTH pneumatic hammers by a weighted pseudo-gradient search Method. *J Mech Des Trans ASME*. 1998;120(4): 687–694. <https://doi.org/10.1115/1.2829332>.
- Song C, Chung J, Cho JS, Nam YJ. Optimal design parameters of a percussive drilling system for efficiency improvement. *Adv Mater Sci Eng*. 2018;2018. <https://doi.org/10.1155/2018/2346598>.
- Lundberg B, Collet P. Optimal wave with respect to efficiency in percussive drilling with integral drill steel. *Int J Impact Eng*. 2010;37(8):901–906. <https://doi.org/10.1016/j.ijimpeng.2010.02.001>.
- Song X, Kane A, Aamo O, Detournay E. A dynamic model of the drilling action of percussive tools. In: *53rd U.S. Rock Mechanics/Geomechanics Symposium*. American Rock Mechanics Association (ARMA); 2019.
- Li X, Rupert G, Summers DA, Santi P, Liu D. Analysis of impact hammer rebound to estimate rock drillability. *Rock Mech Rock Eng*. 2000;33(1):1–13. <https://doi.org/10.1007/s006030050001>.
- Lundberg B. Energy transfer in percussive rock destruction-I. Comparison of percussive methods. *Int J Rock Mech Min Sci*. 1973;10(5):381–399. [https://doi.org/10.1016/0148-9062\(73\)90024-7](https://doi.org/10.1016/0148-9062(73)90024-7).
- Wu G, Liu K, Hu WR, Li JC, Dehkhoda S, Zhang QB. Quantification of dynamic damage and breakage in granite under confined indentation. *Int J Rock Mech Min Sci*. 2021;144(January). <https://doi.org/10.1016/j.ijrmms.2021.104763>.
- Chen L. *Some Aspects of Rock Breakage by Impact Action*. New South Wales; 1993. <https://doi.org/10.26190/unsworks/7857>.
- Kou SQ, Liu HY, Lindqvist P, Tang CA. Rock fragmentation mechanisms induced by a drill bit. *Symp A Q J Mod Foreign Lit*. 2004;41(3):1–6.
- Saadati M, Weddfelt K, Larsson PL. A spherical indentation study on the mechanical response of selected rocks in the range from very hard to soft with particular interest to drilling application. *Rock Mech Rock Eng*. 2020;53(12):5809–5821. <https://doi.org/10.1007/s00603-020-02242-9>.
- Weddfelt K, Saadati M, Larsson PL. On the load capacity and fracture mechanism of hard rocks at indentation loading. *Int J Rock Mech Min Sci*. 2017;100(December 2016):170–176. <https://doi.org/10.1016/j.ijrmms.2017.10.001>.

12. Chiang LE, Elias DA. Modeling impact in down-the-hole rock drilling. *Int J Rock Mech Min Sci.* 2000;37(4):599–613. [https://doi.org/10.1016/S1365-1609\(99\)00124-0](https://doi.org/10.1016/S1365-1609(99)00124-0).
13. Liu K, Zhang QB, Zhao J. Dynamic increase factors of rock strength. In: *Rock Dynamics - Experiments, Theories and Applications - Proceedings of the 3rd International Conference on Rock Dynamics and Applications.* ROCODYN-3.; 2018:169–174.
14. Zhang QB, Zhao J. Quasi-static and dynamic fracture behaviour of rock materials: phenomena and mechanisms. *Int J Fract.* 2014;189(1):1–32. <https://doi.org/10.1007/s10704-014-9959-z>.
15. Zhang ZX, Kou SQ, Jiang LG, Lindqvist PA. Effects of loading rate on rock fracture: fracture characteristics and energy partitioning. *Int J Rock Mech Min Sci.* 2000;37(5):745–762. [https://doi.org/10.1016/S1365-1609\(00\)00008-3](https://doi.org/10.1016/S1365-1609(00)00008-3).
16. Zhang QB, Zhao J. A review of dynamic experimental techniques and mechanical behaviour of rock materials. *Rock Mech Rock Eng.* 2014;47(4):1411–1478. <https://doi.org/10.1007/s00603-013-0463-y>.
17. Huang S. Mechanism of Crushing of Rocks under Dynamic Loading. Thesis. <https://hdl.handle.net/1807/76473>.
18. Zhang ZX. Estimate of loading rate for a TBM machine based on measured cutter forces. *Rock Mech Rock Eng.* 2004;37(3):239–248. <https://doi.org/10.1007/s00603-004-0025-4>.
19. Saksala T, Gomom D, Hokka M, Kuokkala VT. Numerical and experimental study of percussive drilling with a triple-button bit on Kuru granite. *Int J Impact Eng.* 2014;72:56–66. <https://doi.org/10.1016/j.ijimpeng.2014.05.006>.
20. Bu C, Qu Y, Cheng Z, Liu B. Numerical simulation of impact on pneumatic DTH hammer percussive drilling. *J Earth Sci.* 2009;20(5):868–878. <https://doi.org/10.1007/s12583-009-0073-5>.
21. Aldannawy H, Rouabhi A, Gerbaud L. Percussive drilling: experimental and numerical investigations. *Rock Mech Rock Eng.* 2022;55(3):1555–1570. <https://doi.org/10.1007/s00603-021-02707-5>.
22. Baranowski P, Gieleta R, Malachowski J, Damaziak K, Mazurkiewicz L. *Split Hopkinson Pressure Bar impulse experimental measurement with numerical validation.* 2014;(February). <https://doi.org/10.2478/mms-2014-0005>.
23. Karlsson LG, Lundberg B, Sundin KG. Experimental study of a percussive process for rock fragmentation. *Int J Rock Mech Min Sci.* 1989;26(1):45–50. [https://doi.org/10.1016/0148-9062\(89\)90524-X](https://doi.org/10.1016/0148-9062(89)90524-X).
24. Aldannawy HA, Gerbaud L, Rouabhi A. On the influence of tool shape on percussive drilling in hard rocks. In: *55th US Rock Mech/Geomech Symp 2021.* vol. 1. 2021:517–526.
25. Mardoukhi A, Hokka M, Kuokkala V, Tapi. Experimental study of the dynamic indentation damage in thermally shocked granite. *Raken Mek.* 2018;51(1):10–26. <https://doi.org/10.23998/rm.69036>.
26. Ramesh KT. High strain rates and impact experiments. In: *Handbook of Experimental Solid Mechanics.* 2008:1–30.
27. Jiang H, Cai Z, Zhao H. Numerical study of hard rock breakage under indenter impact by the hybrid FDEM. *Eng Fract Mech.* 2020;233(April), 107068. <https://doi.org/10.1016/j.engfractmech.2020.107068>.
28. Jiang H, Cai Z, Wang O, Meng D. Experimental and numerical investigation of hard rock breakage by indenter impact. *Shock Vib.* 2020;2020. <https://doi.org/10.1155/2020/2747830>.
29. Hustrulid WA, Fairhurst C. A theoretical and experimental study of the percussive drilling of rock Part II-force-penetration and specific energy determinations. *Int J Rock Mech Min Sci.* 1971;8(4):335–356. [https://doi.org/10.1016/0148-9062\(71\)90046-5](https://doi.org/10.1016/0148-9062(71)90046-5).
30. Fourmeau M, Kane A, Hokka M. Experimental and numerical study of drill bit drop tests on Kuru granite. *Philos Trans R Soc A Math Phys Eng Sci.* 2017;375(2085). <https://doi.org/10.1098/rsta.2016.0176>.
31. Narisetti C. Quantification of Damage in Selected Rocks Due to Impact with Tungsten Carbide Bits. Toronto. <https://hdl.handle.net/1807/43266>.
32. Lawn B, Wilshaw R. Indentation fracture: principles and applications. *J Mater Sci.* 1975;10(6):1049–1081. <https://doi.org/10.1007/BF00823224>.
33. Song X, Aamo OM, Kane PA, Detournay E. Influence of weight-on-bit on percussive drilling performance. *Rock Mech Rock Eng.* 2021;54(7):3491–3505. <https://doi.org/10.1007/s00603-020-02232-x>.
34. Lindqvist PA, Hai-Hui L. Behaviour of the crushed zone in rock indentation. *Rock Mech Rock Eng.* 1983;16(3):199–207. <https://doi.org/10.1007/BF01033280>.
35. Reyes, et al. *Cuttings analysis for rotary drilling penetration mechanisms and performance evaluation.* In: *49th US Rock Mechanics/Geomechanics Symposium.* vol. 2. 2015:1498–1505.
36. Cook RF, Pharr GM. Direct observation and analysis of indentation cracking in glasses and ceramics. *J Am Ceram Soc.* 1990;73(4):787–817. <https://doi.org/10.1111/j.1151-2916.1990.tb05119.x>.
37. Liu HY, Kou SQ, Lindqvist PA. Numerical studies on bit-rock fragmentation mechanisms. *Int J GeoMech.* 2008;8(1):45–67. [https://doi.org/10.1061/\(asce\)1532-3641\(2008\)8:1\(45\)](https://doi.org/10.1061/(asce)1532-3641(2008)8:1(45)).
38. Lawn BR, Swain MV. Microfracture beneath point indentations in brittle solids. *J Mater Sci.* 1975;10(1):113–122. <https://doi.org/10.1007/BF00541038>.
39. Saksala T. Numerical modelling of bit-rock fracture mechanisms in percussive drilling with a continuum approach. *Int J Numer Anal Methods GeoMech.* 2011;30(35):1483–1505. <https://doi.org/10.1002/nag.974>.
40. Chiang SS, Marshall DB, Evans AG. The response of solids to elastic/plastic indentation. I. Stresses and residual stresses. *J Appl Phys.* 1982;53(1):298–311. <https://doi.org/10.1063/1.329930>.
41. Kou SQ, Xiangchun T, Lindqvist PA. *Modelling of Excavation Depth and Fractures in Rock Caused by Tool Indentation.* 1977.
42. Kou SQ, Liu HY, Lindqvist PA, Tang CA. Rock fragmentation mechanisms induced by a drill bit. *Int J Rock Mech Min Sci.* 2004;41(3):460. <https://doi.org/10.1016/j.ijrmmms.2003.12.127>.
43. Chiang LE. Dynamic force-penetration curves in rock by matching theoretical to experimental wave propagation response. *Exp Mech.* 2004;44(2):167–175. <https://doi.org/10.1177/0014485104042449>.
44. Hashiba K, Fukui K, Liang YZ, Koizumi M, Matsuda T. Force-penetration curves of a button bit generated during impact penetration into rock. *Int J Impact Eng.* 2015;85:45–56. <https://doi.org/10.1016/j.ijimpeng.2015.06.007>.
45. Hustrulid WA, Fairhurst C. A theoretical and experimental study of the percussive drilling of rock part I—theory of percussive drilling. *Int J Rock Mech Min Sci Geomech Abstr.* 1971;8(4):311–333. [https://doi.org/10.1016/0148-9062\(71\)90045-3](https://doi.org/10.1016/0148-9062(71)90045-3).
46. Ulusay R, ed. *The ISRM Suggested Methods for Rock Characterization, Testing and Monitoring.* 2015:2007–2014. <https://doi.org/10.1007/978-3-319-07713-0>.
47. Kaiser M a, Wicks Dr Alfred, Wilson Leonard, Saunders Dr William. *Advancements in the split Hopkinson bar test.* *Mech Eng.* 1998:94. Master.
48. Panowicz R, Konarzewski M. Influence of imperfect position of a striker and input bar on wave propagation in a split Hopkinson pressure bar (SHPB) setup with a pulse-shape technique. *Appl Sci.* 2020;10(7). <https://doi.org/10.3390/app10072423>.
49. Teale R. The concept of specific energy in rock drilling. *Int J Rock Mech Min Sci.* 1965;2(1):57–73. [https://doi.org/10.1016/0148-9062\(65\)90022-7](https://doi.org/10.1016/0148-9062(65)90022-7).
50. Souissi S, Hamdi E, Sellami H. Microstructure effect on hard rock damage and fracture during indentation process. *Geotech Geol Eng.* 2015;33(6):1539–1550. <https://doi.org/10.1007/s10706-015-9920-6>.
51. Saksala T, Fourmeau M, Kane PA, Hokka M. 3D finite elements modelling of percussive rock drilling: estimation of rate of penetration based on multiple impact simulations with a commercial drill bit. *Comput Geotech.* 2018;99(October 2017):55–63. <https://doi.org/10.1016/j.compgeo.2018.02.006>.
52. Izquierdo LE, Chiang LE. A methodology for estimation of the specific rock energy index using corrected down-the-hole drill monitoring data. *Inst Min Metall Trans Sect A Min Technol.* 2004;113(4):225–236. <https://doi.org/10.1179/037178404225006218>.
53. Abu Bakar MZ, Butt IA, Majeed Y. Penetration rate and specific energy prediction of rotary-percussive drills using drill cuttings and engineering properties of selected rock units. *J Min Sci.* 2018;54(2):270–284. <https://doi.org/10.1134/S106273911802363X>.
54. Song H, Shi H, Yuan G, Xia Y, Li J, Liu T. Experimental study of the energy transfer efficiency and rock fragmentation characteristics in percussive drilling. *Geothermics.* 2022;105(April), 102497. <https://doi.org/10.1016/j.geothermics.2022.102497>.
55. Shangxin F, Yujie W, Guolai Z, et al. Estimation of optimal drilling efficiency and rock strength by using controllable drilling parameters in rotary non-percussive drilling. *J Pet Sci Eng.* 2020;193(May), 107376. <https://doi.org/10.1016/j.petrol.2020.107376>.
56. Song CH, Kwon KB, Cho MG, Oh JY, Shin DY, Cho JW. Development of lab-scale rock drill apparatus for testing performance of a drill bit. *Int J Precis Eng Manuf.* 2015;16(7):1405–1414. <https://doi.org/10.1007/s12541-015-0185-z>.
57. Saadati M, Forquin P, Weddfelt K, Larsson PL. On the tensile strength of granite at high strain rates considering the influence from preexisting cracks. *Adv Mater Sci Eng.* 2016;2016. <https://doi.org/10.1155/2016/6279571>.

Nomenclature

Latin

- A_p : Cross sectional area of the piston
 A_b : Cross sectional area of the bit
 c : Wave speed in steel = 5200 m/s
 E_p : Impact energy
 L_p : Piston length
 L_b : Bit length
 L_1 : Distance from strain gauges to the rock surface
 m_b : Bit mass
 m_p : Piston mass
 t_0 : Time at which the incident pulse arrives at the carbide end: Start of the indentation and reaction of the rock
 t_r : Time at which the first reflected wave, carrying information about the reaction of the rock, arrives at the strain gauges
 t_p : Time at which the maximum stress occurs
 t_e : Time early than t_p at which the slope of the bit stress signal change
 t_1 : Time at which radial cracks are first observed on the rock surface
 t_2 : Time at which large fragments are first observed to form on the rock surface
 t_{im} : Time at which the indentation is maximum
 t_{ij} : Time at which the bit-rock interaction ends
 t_{end} : Time at which the whole indentation process ends
 u_f : Penetration depth
 u_m : Maximum indentation
 V_{pi} : Piston impact velocity, impact velocity
 V_{br} : Bit unloading velocity
 $V_{br'}$: Bit unloading velocity after re-contact
 V_{pr} : Piston rebound velocity
 $V_{pr'}$: Piston rebound velocity after re-contact
 Z_p : Piston mechanical impedance

Z_b : Bit mechanical impedance

Greek

k : Apparent rock stiffness

ρ : Density steel = 7850 kg/m³

σ_i : The magnitude of the incident pulse in the bit

σ_m : Maximum stress in the bit (without considering the incident pulse)

σ_r : Stress in the bit at t_r

τ : Time length of the incident pulse

Acronyms

DTH: Down The Hole

FDEM: Finite-Discrete Element Method

ISRM: International Society for Rock Mechanics

SE: Specific Energy

SHPB: Split Hopkinson Pressure Bar

THD: Top Hammer Drill

UCS: Unconfined Compressive Strength

UTS: Unconfined Tensile Strength

WOB: Weight On Bit